Available online at www.sciencedirect.com
SCIENCE DIRECT®
Polymer 44 (2003) 5859–5866
polymer
www.elsevier.com/locate/polymer

Parallel algorithm for numerical self-consistent field theory simulations of block copolymer structure

Scott W. Sides*, Glenn H. Fredrickson

Chemical Engineering II, Chemical Engineering, University of California at Santa Barbara (UCSB), Santa Barbara, CA 93106, USA

Received 22 May 2003; accepted 2 July 2003

Abstract

An efficient algorithm is presented for numerically evaluating a self-consistent field theoretic (SCFT) model of block copolymer structure. This algorithm is implemented on a distributed memory parallel cluster in order to solve the SCFT equations on large computational grids. Simulation results are presented for a two-component molten mixture of a symmetric ABA triblock copolymer with an A homopolymer. These results illustrate a case in which simulating a large system is required to resolve features with a wide range of length scales.

PACS: 61.25.Hq; 61.43.Bn; 64.75. + g; 64.60.Cn; 64.70.Nd

Keywords: Block copolymers; Self-consistent field theory

1. Introduction

Block copolymers are an important class of materials that are employed in colloidal stabilization [1,2], as adhesives, and as thermoplastic elastomers. In another application, the adhesion between two glassy, incompatible homopolymer melts can be strengthened [3–5] by the addition of diblock copolymers that organize near the interface. Blends of homopolymers can also be stabilized by the addition of block copolymers [6] and can form bi-continuous micro-emulsions [7]. The morphologies of pure block copolymer systems observed in experiments [8] and predicted by simulations [9] suggest many exciting possibilities for creating novel and potentially useful soft material nanostructures and templates.

Self-consistent field theory (SCFT) for dense polymer melts [10,11] has been highly successful in describing complex morphologies in block copolymers. SCFT provides a method whereby the Hamiltonian of a complex system may be transformed into a coarse-grained field theory description, whose mean-field solution is amenable to a battery of analytic and numerical methods. Matsen and Schick [12] have solved the SCFT equations with a 'spectral' method that can calculate very accurate free-energies, but requires foreknowledge of the preferred symmetry for each structural phase. Recently, a 'real space' numerical method has been used to solve the SCFT equations [9,13,14] which does not need any information about the equilibrium morphologies. This numerical SCFT method is more flexible than the spectral method and has a greater predictive capability, however, it is computationally intensive and requires large memory resources.

For a single-component, monodisperse copolymer, the ordered structures are periodic and have a size on the order of the radius of gyration of the unperturbed chain. These cases require simulating relatively small systems in order to resolve the relevant length scale. However, for multi-component mixtures or systems with chemical disorder, a range of widely separated length scales could be germane to fully describing equilibrium morphologies and will require the use of large simulation cells. The present work is aimed at providing a computational methodology appropriate for such systems. Section 2 contains an outline of SCFT for polymers. Section 3 briefly describes the numerical implementation of the theory including details on the parallelization algorithm. Results for a triblock/homopolymer mixture are discussed in Section 4 followed by conclusions in Section 5.

* Corresponding author. Tel.: +1-805-8937669; fax: +1-805-8934731.
E-mail address: swsides@mrl.ucsb.edu (S.W. Sides).

0032-3861/03/$ - see front matter © 2003 Elsevier Ltd. All rights reserved.
doi:10.1016/S0032-3861(03)00606-2

2. SCFT theory for polymers

We briefly describe the model and simulation method used to predict the structure of a dense melt of AB diblock copolymers. The method is easily generalized to treat the ABA triblock/A homopolymer mixtures considered in this paper. The Hamiltonian for a dense system of polymer chains comprised of blocks containing chemically distinct monomers A and B is

$$H = \frac{1}{4R_{g0}^2}\sum_{\alpha=1}^{n}\int_0^1 \mathrm{d}s\left(\frac{\mathrm{d}\vec{r}_\alpha(s)}{\mathrm{d}s}\right)^2 + \rho_0^{-1}\int \mathrm{d}\vec{r}\ \chi\ \hat{\rho}_A(\vec{r})\hat{\rho}_B(\vec{r}) \quad (1)$$

The first term in H is the free-energy contribution from the so-called 'Gaussian thread' [15] model. This term can be derived as the continuous limit of a chain model consisting of coarse-grained, spherical beads connected by harmonic springs, where R_{g0} is the radius of gyration for the unperturbed Gaussian chain, n is the number of chains and $\vec{r}_\alpha(s)$ is a space curve parameterized by the chain contour variable s which describes the configuration of the αth chain. The second term is obtained from a Flory-type model of the interaction energy between chemically distinct monomer species A and B, which is parameterized by χ. The total monomer density is $\rho_0 = nN/V$, where N is the polymerization index and V is the volume. For these simulations $\chi > 0$ indicating an overall repulsive force between dissimilar monomers which drives phase separation. Note that while χ is known experimentally to depend on temperature, there is no such explicit dependence in the present theoretical formulation. The predictions for the mesoscopic structure of the triblock system studied in this paper are for particular values of χ, which depend not only on the specific interactions between chemical species A and B, but on the temperature as well.

The monomer density operators for the A and B species are

$$\hat{\rho}_A(\vec{r}) = N\sum_{\alpha=1}^{n}\int_0^f \mathrm{d}s\ \delta(\vec{r} - \vec{r}_\alpha(s)) \quad (2)$$

$$\hat{\rho}_B(\vec{r}) = N\sum_{\alpha=1}^{n}\int_f^1 \mathrm{d}s\ \delta(\vec{r} - \vec{r}_\alpha(s)) \quad (3)$$

where f is the fraction of the chain consisting of A monomers. The partition function for this system can be written as

$$Z = \int \prod_{\alpha=1}^{n} \tilde{D}\vec{r}_\alpha \exp\left\{-\rho_0^{-1}\int \mathrm{d}\vec{r}\ \chi\ \hat{\rho}_A(\vec{r})\hat{\rho}_B(\vec{r})\right\}\delta[\rho_0 - \hat{\rho}_A - \hat{\rho}_B] \quad (4)$$

with

$$\tilde{D}\vec{r}_\alpha = D\vec{r}_\alpha \exp\left\{-\frac{1}{4R_{g0}^2}\int_0^1 \mathrm{d}s\left(\frac{\mathrm{d}\vec{r}_\alpha(s)}{\mathrm{d}s}\right)^2\right\} \quad (5)$$

where $\int D\vec{r}_\alpha$ denotes a path integral over all possible conformations of the αth chain and the delta function enforces an incompressibility constraint between A and B monomers such that the total monomer density is kept constant. The partition function is now expressed in terms of monomer density operators which enumerate the positions of the A/B monomers on the n polymer chains. This expression for Z may be converted into a field-theoretic description by a Hubbard–Stratonovich (HS) transformation by insertion of the functional integral identity

$$\begin{aligned} 1 &= \int D[\rho]\ \delta[\rho - \hat{\rho}] \\ &= \int D[\rho]\ D[\omega]\exp\left\{\int \mathrm{d}\vec{r}\ \mathrm{i}w(\vec{r})[\rho(\vec{r}) - \hat{\rho}(\vec{r})]\right\} \end{aligned} \quad (6)$$

where the chemical potential field $w(\vec{r})$ has been introduced through the exponential representation of the delta functional $\delta[\rho - \hat{\rho}]$. Using the identity in Eq. (6) for both A and B density operators and substituting the exponential form of the incompressibility constraint gives

$$Z = \int D\rho_A D\rho_B D\omega_A D\omega_B Dp\ \mathrm{e}^{-\beta F} \quad (7)$$

$$\beta F = \int \mathrm{d}\vec{r}[\rho_0^{-1}\chi\rho_A\rho_B - \mathrm{i}w_A\rho_A - \mathrm{i}w_B\rho_B - \mathrm{i}p(\rho_0 - \rho_A - \rho_B)] - n\ln Q[\mathrm{i}w_A, \mathrm{i}w_B; N] \quad (8)$$

with

$$Q = \frac{\int \tilde{D}\vec{r}_\alpha \exp\left\{-\int_0^f \mathrm{d}s\ \mathrm{i}Nw_A(\vec{r}_\alpha(s)) - \int_f^1 \mathrm{d}s\ \mathrm{i}Nw_B(\vec{r}_\alpha(s))\right\}}{\int \tilde{D}\vec{r}_\alpha} \quad (9)$$

The field p is a 'pressure field' introduced to enforce incompressibility and Q is the single-chain partition function which is a functional of the chemical potential fields w_A, w_B and a function of the chain length N. The explicit $\vec{r}$ dependence is ignored for brevity and 'ideal gas' terms of order $\ln V$ have been dropped as they merely add a constant shift in the free-energy. The equation for Q is analogous to the Feynman–Kac formula in the path-integral description of quantum mechanics [16] and may be expressed as

$$Q = V^{-1}\int \mathrm{d}\vec{r}\ q(\vec{r}, 1) \quad (10)$$

where $q(\vec{r}, s)$ is a restricted chain partition function that may be calculated as the solution to the modified diffusion equation

$$\frac{\partial q}{\partial s} = \begin{cases} R_{g0}^2\nabla^2 q(\vec{r}, s) - \mathrm{i}Nw_A q(\vec{r}, s), & 0 < s < f \\ R_{g0}^2\nabla^2 q(\vec{r}, s) - \mathrm{i}Nw_B q(\vec{r}, s), & f < s < 1 \end{cases} \quad (11)$$

subject to the initial condition $q(\vec{r}, 0) = 1$. The HS transformation has allowed the discrete density operators $\hat{\rho}$ to be replaced by the 'smeared out' density fields ρ and

permits the chain–chain interactions present in Eq. (4) to be reformulated in terms of a single chain interacting with the chemical potential fields w_A and w_B.

However, the functional integrals in Eq. (7) are still analytically intractable, so a numerical simulation is required. Here, we consider a mean-field approximation where the full partition function is approximated by its value when the fields attain their 'saddle-point' values. For field-theoretic polymer models such as the one presented here, it is known that [14] the equilibrium saddle-points are located along the imaginary axis in the complex-w plane. Hence, the following fields may be rescaled as $\omega_A = iNw_A$, $\omega_B = iNw_B$, and $p = iNp$ with ω_A, and ω_B and p purely real. The simulation results of all density configurations in the phase-separated block copolymer systems will be presented in terms of the dimensionless monomer volume fraction $\phi_i = \rho_i/\rho_0$ for each species i. Rescaling the free-energy by $N/\rho_0 V$ and shifting so that $F - F_0 = 0$ for $\omega_i = 0$ (where F_0 is the free-energy of the disordered phase), gives the free-energy per chain as

$$\tilde{F} = V^{-1}\int d\vec{r}[\chi N(\phi_A - \bar{\phi}_A)(\phi_B - \bar{\phi}_B) - \omega_A\phi_A - \omega_B\phi_B - p(1 - \phi_A - \phi_B)] - \ln Q[\omega_A, \omega_B] \tag{12}$$

where $\bar{\phi}_A[\bar{\phi}_B]$ is the average volume fraction of the A[B] species respectively. The value of the fields $[\phi_A, \phi_B, \omega_A, \omega_B, p]$ at the saddle-point satisfy the following set of equations

$$\omega_A(\vec{r}) = \chi N(\phi_B(\vec{r}) - \bar{\phi}_B) + p(\vec{r}) \tag{13}$$

$$\omega_B(\vec{r}) = \chi N(\phi_A(\vec{r}) - \bar{\phi}_A) + p(\vec{r}) \tag{14}$$

$$\phi_A(\vec{r}) + \phi_B(\vec{r}) = 1 \tag{15}$$

$$\phi_A(\vec{r}) = -\frac{V}{Q}\frac{\delta Q}{\delta\omega_A} \tag{16}$$

$$\phi_B(\vec{r}) = \frac{V}{Q}\frac{\delta Q}{\delta\omega_B} \tag{17}$$

Using a well-known factorization of the single-chain path integral [10,16,17] the functional derivatives in Eqs. (16) and (17) may be rewritten, resulting in the following expressions for the A and B monomer density fractions

$$\phi_A(\vec{r}) = \frac{1}{Q}\int_0^f ds\, q(\vec{r}, s)\, q^\dagger(\vec{r}, s) \tag{18}$$

$$\phi_B(\vec{r}) = \frac{1}{Q}\int_1^1 ds\, q(\vec{r}, s)\, q^\dagger(\vec{r}, s) \tag{19}$$

where the solution to the restricted partition function $q^\dagger$, may be calculated as the solution to a modified diffusion equation similar to Eq. (11) subject to the initial condition $q^\dagger(\vec{r}, 1) = 1$ [12].

3. Numerical SCFT algorithm

3.1. Calculating saddle-points

Eqs. (13)–(17) must be solved self-consistently to determine the saddle-point configurations of the fields $[\phi_A, \phi_B, \omega_A, \omega_B, p]$. We want to devise an iterative procedure whereby the fields may be relaxed towards their saddle-point values. Since one is concerned only with the equilibrium values for the fields, the intermediate field values are not required to describe any sort of realistic dynamics during the relaxation algorithm. Hence, the chemical potential fields ω_A, ω_B may be treated as the relevant dynamical variables with the changes in the ϕ_A, ϕ_B and p fields treated as fast modes and, at each relaxation step, slaved to the values of the chemical potentials. Following the work of Drolet and Fredrickson [9,14] we employ a 'model A' type relaxation dynamics [18] for finding the saddle-point configurations of the fields. This results in the following expressions for updating the chemical potential fields from relaxation step n to $n + 1$

$$\begin{aligned}\omega_A^{n+1} - \omega_A^n &= \lambda'\frac{\delta\tilde{F}}{\delta\phi_B^n} + \lambda\frac{\delta\tilde{F}}{\delta\phi_A^n}\\ &= \lambda'\left[\phi_A^n - \bar{\phi}_A - \frac{\omega_B^n - p^n}{\chi N}\right]\\ &\quad + \lambda\left[\phi_B^n - \bar{\phi}_B - \frac{\omega_A^n - p^n}{\chi N}\right]\end{aligned} \tag{20}$$

$$\begin{aligned}\omega_B^{n+1} - \omega_B^n &= \lambda\frac{\delta\tilde{F}}{\delta\phi_B^n} + \lambda'\frac{\delta\tilde{F}}{\delta\phi_A^n}\\ &= \lambda\left[\phi_A^n - \bar{\phi}_A - \frac{\omega_B^n - p^n}{\chi N}\right]\\ &\quad + \lambda'\left[\phi_B^n - \bar{\phi}_B - \frac{\omega_A^n - p^n}{\chi N}\right]\end{aligned} \tag{21}$$

where the relaxation parameters are chosen such that $\lambda' < \lambda$ and $\lambda > 0$ and the quantities ϕ_A^n, ϕ_B^n are calculated as functionals of ω_A^n, ω_B^n using Eqs. (18) and (19). The relaxation scheme for calculating the saddle-point values for the fields is implemented through the following steps:

1. random initial values are set for ω_A, ω_B and p,
2. the modified diffusion equations are solved numerically to calculate $q(\vec{r}, s)$ and $q^\dagger(\vec{r}, s)$,
3. these functions are substituted into Eqs. (18) and (19) to obtain ϕ_A^n, ϕ_B^n,
4. the expressions in Eqs. (20) and (21) are used to update the chemical potential fields at the n-th iteration, ω^n, to their values at the $(n + 1)$-th iteration, ω^{n+1},
5. the pressure field is updated using the expression $p^{n+1} = (\omega_A^{n+1} + \omega_B^{n+1})/2$.

After updating the pressure field, its spatial average

$V^{-1}\int p(\vec{r})\mathrm{d}\vec{r}$ is subtracted so as to improve the algorithm's stability. This has no effect on the equilibrium structure of the chains as the thermodynamic properties are invariant to a constant shift in the pressure field. With the new fields ω_A, ω_B and p the procedure returns to step 2 and is repeated until the saddle-point configurations are found.

3.2. Parallel algorithm

The most computationally demanding step in the SCFT algorithm outlined in Section 3.1 is in obtaining the solutions for the restricted partition functions q and $q^\dagger$. Finding these solutions requires solving Eq. (11) every time the chemical potential fields ω_A and ω_B are updated. To relax these fields to the saddle-point configurations can require on the order of 10^3–10^4 iterations; hence, an efficient method for solving the modified diffusion equations for $q(\vec{r},s)$ and $q^\dagger(\vec{r},s)$ is essential. We have tried various finite-difference algorithms including explicit and implicit schemes [19] for solving partial differential equations. Implicit schemes such as Crank–Nicholson are more stable and accurate than the simple forward-time centered-space explicit scheme. However, the Crank–Nicholson scheme is only conditionally stable in three dimensions and is not straightforward to implement on a distributed memory computer cluster. More sophisticated explicit schemes such as the Dufort–Frankel algorithm are unconditionally stable in two and three dimensions and are more readily amenable to parallelization. Still, this scheme has accuracy restrictions which limit the size of the contour step Δs that can be used.

In a recent paper [20], a pseudo-spectral (PS) algorithm was used to solve the modified diffusion equations in SCFT theory for calculating block-copolymer structure. This method is unconditionally stable in all dimensions and has superior accuracy to the finite-difference algorithms referenced above. The derivation of the PS algorithm starts with the exact expression for propagating the solution at $q(\vec{r},s)$ to $q(\vec{r},s+\Delta s)$

$$q(\vec{r},s+\Delta s)=\exp\left[\Delta s(\nabla^2-w(\vec{r}))\right]q(\vec{r},s) \tag{22}$$

If the time propagator above is expanded and terms of order $(\Delta s)^3$ are ignored, the remaining terms can be rewritten as

$$q(\vec{r},s+\Delta s)\approx \mathrm{e}^{-w(\vec{r})\Delta s/2}\,\mathrm{e}^{\Delta s\nabla^2}\,\mathrm{e}^{-w(\vec{r})\Delta s/2}\,q(\vec{r},s) \tag{23}$$

$$q(\vec{r},s+\Delta s)\approx \mathrm{e}^{-w(\vec{r})\Delta s/2}\,\hat{F}^{-1}\left[\mathrm{e}^{-\Delta s k^2}\,\hat{F}[\mathrm{e}^{-w(\vec{r})\Delta s/2}\,q(\vec{r},s)]\right] \tag{24}$$

The first exponential factor depending on $\omega(\vec{r})/2$ is applied in real space to $q(\vec{r},s)$. The Fourier transform $\hat{F}$ is applied to this result and then the operator $\exp[\Delta s\nabla^2]$ can be applied exactly in reciprocal space as $\exp(-\Delta s k^2)$ for a given discretization of the chemical potential fields ω and restricted partition functions $q(\vec{r},s)$. The inverse Fourier transform $\hat{F}^{-1}$ is applied to this result and the last exponential factor is again applied in real space. Since two Fourier transforms must be applied to calculate $q(\vec{r},s)$ for each contour step s, an efficient Fourier transform algorithm is essential. The publicly available FFTW [21] fast-Fourier transform libraries were employed in the numerical SCFT code used to obtain the results in this paper.

The unconditional stability and improved accuracy of the PS algorithm allows for fewer spectral elements and a larger Δs to be used, relative to finite-difference methods. Therefore, fewer contour steps are needed to solve for $q(\vec{r},s)$ from $s=0$ to $s=1$ resulting in decreased computation times. For very large systems, the SCFT algorithm has been parallelized enabling implementation on a distributed memory cluster of computers. Fig. 1 shows a diagram of a computational grid used to discretize the fields $\omega_A(\vec{r})$, $\omega_B(\vec{r})$, $\phi_A(\vec{r})$, $\phi_B(\vec{r})$ as well as the functions $q(\vec{r},s)$, $q^\dagger(\vec{r},s)$. This diagram illustrates a spatial, domain decomposition scheme in which separate regions of the computational lattice are assigned to distinct processors. All variables, including those regions of the computational grid shown in Fig. 1, that have unique values corresponding to a distinct processor (or node) will be referred to as 'local'. Variables that have the same values on all processors or refer to overall system parameters will be referred to as 'global'. Each processor performs computations on its local data, and uses MPI communication between nodes when a computation requires data, which is local to another processor. The steps in the SCFT algorithm outlined in Section 3.1 are

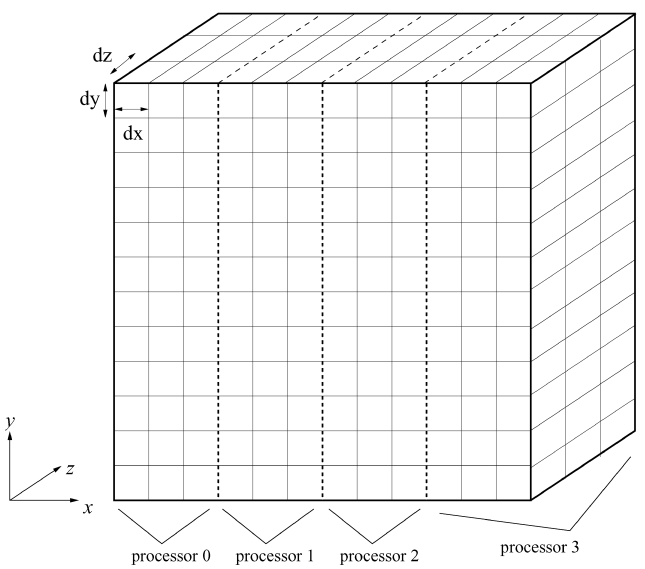

Fig. 1. Spatial domain decomposition scheme for solving the SCFT equations on a distributed-memory computer cluster. This schematic diagram shows the computational grid used to discretize the fields $\omega_A(\vec{r})$, $\omega_B(\vec{r})$, $\phi_A(\vec{r})$, $\phi_B(\vec{r})$ as well as the functions $q(\vec{r},s)$, $q^\dagger(\vec{r},s)$. Each processor is assigned a "slab" portion of the grid, of size $L_x/(N_p)\times L_y\times L_z$ where N_p is the number of processors. The size of the grid spacing ($\mathrm{d}x=\mathrm{d}y=\mathrm{d}z$) is in units of R_g, the radius of gyration for the unperturbed Gaussian chain. This domain decomposition scheme is easily adapted to 2D and 3D, any number of processors and larger systems.

parallelized by identifying the steps requiring only local computation, and the steps which also include inter-processor communication via MPI.

After initializing all fields, step 2 in Section 3.1 requires solving modified diffusion equations, whose solutions can be obtained by repeated evaluation of Eq. (24). The action of the real-space operators $\exp(-w(\vec{r})\Delta s/2)$ and the reciprocal space operator $\exp(-\Delta s k^2)$ need only local computation. However, the forward and backward Fourier transforms require both local computation and inter-processor communication. A parallel Fourier transform is performed in an analogous manner as a serial Fourier transform on a multi-dimensional array of data. First, a series of 1-d FFT's in the y and z directions is applied to all local data. Since FFT algorithms (such as the standard Danielson–Lanczos algorithm [22]) require all data in one dimension to be local, this explains the slab decomposition illustrated in Fig. 1. Second, a matrix transpose operation is performed and then another 1d FFT is applied along the remaining x direction. Communication cost is incurred through the matrix transpose, which clearly requires sending and receiving data to and from sections of the computation grid local to different processors. In step 3, Eqs. (18) and (19) are used to compute the monomer density fields ϕ_A, ϕ_B. The integrals over ds are calculated by a simple quadrature algorithm, (using the extended-trapezoidal rule) requiring only local computation. However, the single-chain partition function Q contains an integral over space requiring more inter-processor communication, which is implemented with a simple MPI 'all-to-all' [23] global communication call. The final steps 4 and 5, updating the fields ω_A, ω_B and p from n to $n+1$, require only local computation. Timing results for the parallel SCFT code are shown in Fig. 2(a),(b) for 2D and 3D systems, respectively. The data in these figures represents both the computation/communication time required to solve the diffusion equation with the pseudo-spectral algorithm for 1000 field iterations. Note, that except for I/O, other parts of the SCFT calculation are small in comparison to this contribution to the CPU time. The insets in Fig. 2 show log–log plots of the same timing data with dotted lines indicating the limit of perfect speedup. A decrease in parallel efficiency for small systems is most clearly illustrated in the inset for Fig. 2(b). For the smaller system (32^3), parallel performance is degraded as the number of processors increases. This trend illustrates the increasing ratio of communication-to-computation CPU time as the number of lattice points per processor decreases. Hence, the decrease in parallel efficiency for the larger system in Fig. 2(b) is less pronounced than in the smaller system.

4. Results

Figs. 3 and 4 show the density configurations for a mixture of symmetric triblock copolymer chains and monodisperse homopolymer chains. The outer blocks of the triblock consist of equally sized lengths of polymerized A monomers while the inner block consists of B monomers. The total number of A monomers on each triblock chain is $f_A N_t$ where f_A is the fraction of A monomers/triblock and N_t is the triblock polymerization index. The volume fraction of monomers on homopolymer chains v_h is given by

$$v_h = \frac{n_h N_h}{n_h N_h + n_t N_t} \tag{25}$$

where $n_h(n_t)$ is the number of homopolymer(triblock) chains and N_h is the homopolymer polymerization index. The chain lengths used are $N_h = 100$ and $N_t = 200$. The total density of A monomers is shown in Figs. 3 and 4 with light(dark) regions corresponding to high(low) values of the monomer density volume fraction, $\rho_A(\vec{r})$. With only two chemical species, the incompatibility between them is described by a single Flory parameter, χ_{AB}.

Small values of v_h (on the left of each plot) correspond to a mixture consisting of almost pure triblock while the large values of v_h correspond to a nearly pure homopolymer mixture. For small v_h, the typical phase-separated cylindrical and lamellar ordered structures can be seen with disordered phases for the largest and smallest values of f_A. As homopolymer is added to the pure triblock, the A domains of the triblock begin to swell. For sufficiently large amounts of homopolymer, the A domains of the triblock can stretch no further and macrophase separation occurs with large domains of pure homopolymer appearing. All of these features are in qualitative agreement with SCFT results by Matsen [24] of an AB diblock/A homopolymer mixture. However, these calculations use a spectral method to calculate the SCFT theory and require assumptions about the symmetries of the phase-separated states. The attractiveness of the present pseudo-spectral approach is that it allows for a rapid assessment of phase behavior in complex mixtures characterized by a large number of model parameters.

The density plot shown for $f_A = 0.3$ and $v_h \sim 0.2$ in Fig. 4 shows the two-phase region particularly well. The smallest domains consist primarily of A monomers belonging to triblock chains with a size corresponding to the cylindrical phase in the pure triblock. The larger domains consist mostly of homopolymer chains that have been expelled from the smaller cylindrical phase domains. Additional features have been introduced with length scales larger than the cylindrical triblock domains, such as the spacing between the larger domains and the arrangement of the small domains which is clearly affected by the presence of the phase-separated homopolymer-rich regions.

It should be noted that these density profiles are not the true saddle-point configurations of the fields, but represent local metastable configurations in the vicinity of the equilibrium saddle point. These configurations contain a variety of topological defects which distort pure lamellar order (e.g. $f_A = 0.50$, $v_h \sim 0.05$) as well as perfect,

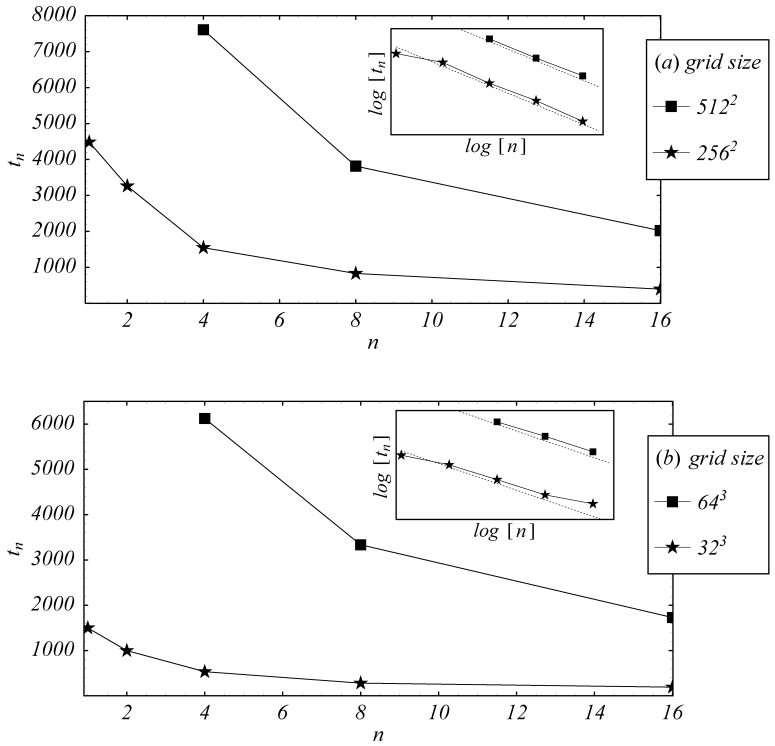

Fig. 2. CPU time t_n vs. number of processors n for (a) 2D systems and (b) 3D systems. The time shown is the total computation and communication time required to solve the diffusion equation using the pseudo-spectral algorithm. This part of the SCFT calculation accounts for the majority of the total CPU time. The insets shows the same timing data on a log–log plot. The dotted lines indicate the limit of perfect speedup and have slopes of -1. Note: for the largest systems, no timing data is available for one and two processors because the job exceeded local memory.

hexagonal ordering for cylindrical domains (e.g. $f_A = 0.70$, $v_h \sim 0.05$). However, 'near-equilibrium' configurations such as these are typically observed in experiments. Moreover, the present simulation strategy has produced defect structures in qualitative agreement with size adjustments observed in 5 and 7-fold coordinated defects in PCHE-PE-PCHE triblock thin films [25]. Fig. 5 shows the SCFT result for a much larger system (1024×1024 lattice) with the same parameters as one of the runs shown in Fig. 4 (i.e. $f_A = 0.30$, $v_h \sim 0.20$). The true equilibrium

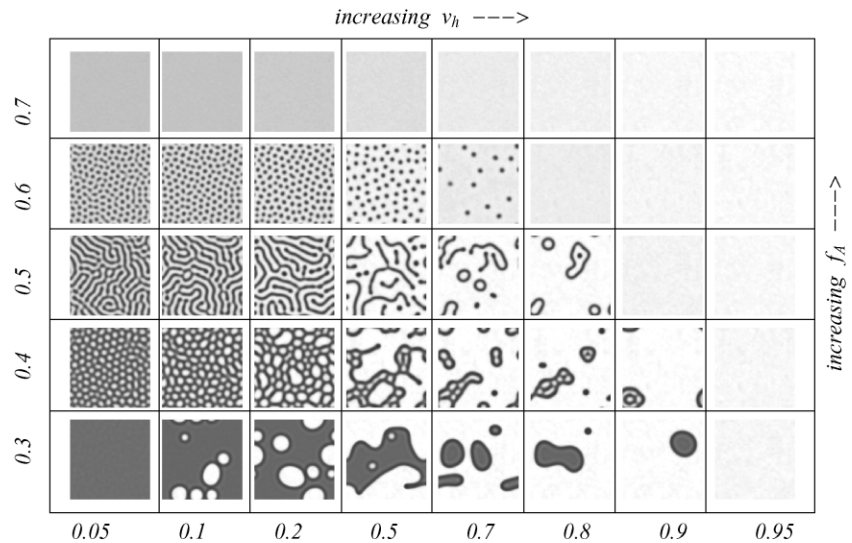

Fig. 3. Density configurations of symmetric ABA triblock/A homopolymer mixtures for $\chi_{AB} = 0.10$. White regions denote a high concentration of A monomers while dark regions denote a high concentration of B monomers. The chain polymerization indexes are $N_t = 200$ and $N_h = 100$. The vertical direction in each figure shows varying amounts of A monomers in the ABA triblock. The horizontal direction shows the volume fraction v_h of monomers on the homopolymer chains in the system. Each of these simulations (i.e. each frame) is obtained running the SCFT code on four processors and shows results on a 128×128 lattice ($32R_g \times 32R_g$).

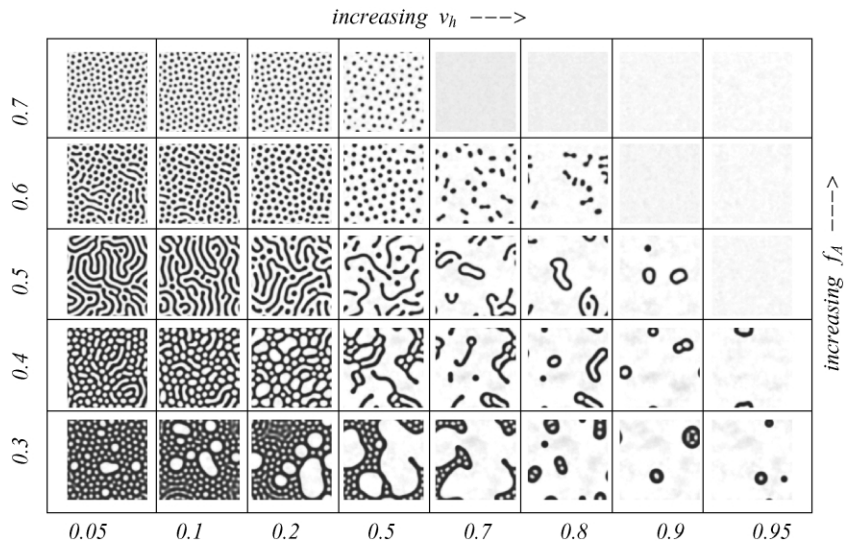

Fig. 4. Density configurations of symmetric ABA triblock/A homopolymer mixtures for $\chi_{AB} = 0.16$. The data is organized in the same way as in Fig. 3. Results for $f_A = 0.30$, $v_h = 0.20$ on a larger simulation lattice are shown in Fig. 5.

configuration for a macrophase separated system would presumably contain a single, homopolymer-rich domain but Fig. 5 shows one possible distribution of sizes and arrangements of smaller, homopolymer-rich domains. The distribution of these smaller domains can be thought of as topological defects in the copolymer mixture that will migrate and very slowly coalesce into a single macroscopic domain as additional iterations of the SCFT algorithm are performed. However the configuration shown in Fig. 5 should correspond to an experimentally realizable structure, as in the triblock thin-film study cited above.

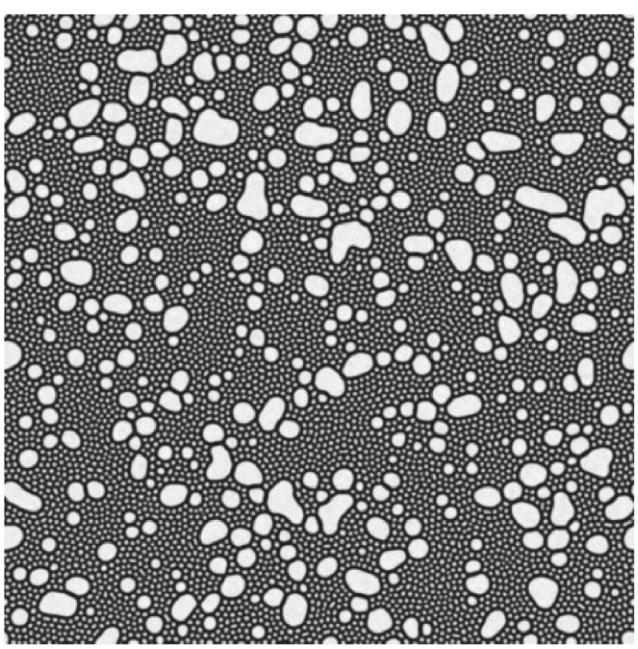

Fig. 5. Density configuration of symmetric ABA triblock/A homopolymer mixture for $f_A = 0.30$, $v_h = 0.20$ and $\chi_{AB} = 0.16$. The same parameters are used in one of the simulation results shown in Fig. 4 for a smaller 128×128 lattice. The result shown here is for a 1024×1024 lattice ($256R_g \times 256\ R_g$).

5. Conclusions

Numerical SCFT has been used to study the complex morphologies present in phase-separated block copolymer systems. We presented an efficient algorithm using a combination of a pseudo-spectral algorithm for solving a modified diffusion equation and parallelization that enables faster and larger simulations. This capability allows investigation of systems where many length scales are needed to fully describe the morphology. A mixture of ABA triblock and A homopolymer is used to benchmark the SCFT algorithm and demonstrate the ability to simultaneously resolve both microphase and macrophase separation. The micellar regimes in the ABA/A mixture could be further studied with a complex Langevin scheme [14] for sampling full, thermodynamic averages within SCFT. If one extends this type of study to 3D systems (in order to resolve the cubic, gyroid and bcc spherical phases), the parallel algorithm presented here will be even more helpful.

Acknowledgements

SW Sides is grateful to Atofina Chemicals for financial support. The authors also acknowledge support from the National Science Foundation under Award Number DMR-98-70785 and extensive use of the UCSB-MRL Central Computing Facilities. Special thanks to Jeffery Barteet for his important role in building the MRL parallel computing cluster.

References

[1] Napper DH. Polymeric stabilization of colloidal dispersions. London: Academic; 1983.

[2] Russell WB, Saville DA, Schowalter WR. Colloidal dispersions. Cambridge: Cambridge University Press; 1989.

[3] Brown HR, Char K, Deline VR, Green PF. Effects of a diblock copolymer on adhesion between immiscible polymers. 1. PS-PMMA copolymer between PS and PMMA. Macromolecules 1993;26:4155.

[4] Kramer EJ, Norton LJ, Dai C-A, Sha Y, Hui C-Y. Strengthening polymer interfaces. Faraday Discuss. 1994;98:31.

[5] Dai C-A, Kramer EJ, Washiyama J, Hui C-Y. Fracture toughness of polymer interface reinforced with diblock copolymer: effect of homopolymer molecular weight. Macromolecules 1996;29:7536.

[6] Riess G, Jolivet Y. In: Platzer NAJ, editor. Polyblends and composites. ACS advances in chemistry series, vol. 142. Washington, DC: American Chemical Society; 1975. p. 243.

[7] Morkved TL, Stepanek P, Krishnan K, Bates FS, Lodge TP. Static and dynamic scattering from ternary polymer blends: bicontinuous microemulsions, lifshitz lines, and amphiphilicity. J. Chem. Phys. 2001;114(16):7247–59.

[8] Hamley IW. The Physics of block copolymers. Oxford: Oxford University Press; 1998.

[9] Drolet F, Fredrickson GH. Combinatorial screening of complex block copolymer assembly with self-consistent field theory. Phys. Rev. Lett. 1999;83(21):4317–20.

[10] Freed KF. Functional integrals and polymer statistics. Adv. Chem. Phys. 1972;22:1.

[11] Hong KM, Noolandi J. Theory of inhomogeneous multicomponent polymer systems. Macromolecules 1981;14:727–36.

[12] Matsen MW, Schick M. Stable and unstable phases of a diblock copolymer melt. Phys. Rev. Lett. 1994;72:2660–3.

[13] Maurits N, Fraaije JGEM. Mesoscopic dynamics of copolymer melts: from density dynamics to external potential dynamics using nonlocal kinetic coupling. J. Chem. Phys. 1997;107(15):5879.

[14] Fredrickson GH, Ganesan V, Drolet F. Field-theoretic computer simulation methods for polymers and complex fluids. Macromolecules 2002;35:16–39.

[15] Doi M, Edwards S. The theory of polymer dynamics. Oxford: Clarendon Press; 1986.

[16] Feynman RP, Hibbs AR. Quantum mechanics and path integrals. New York: McGraw-Hill Book Company; 1965.

[17] Helfand E. Theory of inhomogeneous polymers: fundementals of the gaussian random-walk model. J. Chem. Phys. 1974;62(3):999–1005.

[18] Hohenberg PC, Halperin BI. Theory of dynamic critical phenomena. Rev. Mod. Phys. 1977;49(3):436–75.

[19] Fletcher CAJ, 2nd ed. Computational techniques for fluid dynamics, vol. 1. Berlin: Springer; 1991.

[20] Tzeremes G, Rasmussen KO, Lookman T, Saxena A. Efficient computation of the structural phase behavior of block copolymers. Phys. Rev. E. 2002;65:041806.

[21] Frigo M, Johnson SG. FFTW: an adaptive software architecture for the FFT. Proc. ICASSP 1998;1998(3):1381–4.

[22] Press WH, Teukolsky SA, Vetterling WT, Flannery BP. Numerical Recipes in Fortran: The Art of Scientific Computing, 2nd ed. Boston: Cambridge University Press; 1992.

[23] Pacheco PS. Parallel programming with MPI. San Francisco: Morgan Kaufmann; 1997.

[24] Matsen MW. Stabilizing new morphologies by blending homopolymer with block copolymer. Phys. Rev. Lett. 1995;74:4225–8.

[25] M.R. Hammond, S.W. Sides, G.H. Fredrickson, E.J. Kramer, J. Ruokolainen, S.F. Hahn, Adjustment of block copolymer nanodomain sizes at lattice defect sites, submitted to Macromolecules.